Unveiling the Magnetic Structure of Graphene Nanoribbons

Rebeca Ribeiro,[1] Jean-Marie Poumirol,[1] Alessandro Cresti,[2] Walter Escoffier,[1] Michel Goiran,[1] Jean-Marc Broto,[1] Stephan Roche,[3,4] and Bertrand Raquet[1]

[1]*Laboratoire National des Champs Magnétiques Intenses, INSA UPS UJF CNRS, UPR 3228, Université de Toulouse, 143 av. de Rangueil, 31400 Toulouse, France*

[2]*IMEP-LAHC (UMR CNRS/INPG/UJF 5130), Grenoble INP Minatec, 3 Parvis Louis Néel, BP 257, F-38016 Grenoble, France*

[3]*CIN2 (ICN-CSIC) and Universitat Autonoma de Barcelona, Catalan Institute of Nanotechnology, Campus de la UAB, 08193 Bellaterra (Barcelona), Spain*

[4]*ICREA, Institucio Catalana de Recerca i Estudis Avançats, 08010 Barcelona, Spain*

(Received 7 February 2011; published 19 August 2011)

We perform magnetotransport measurements in lithographically patterned graphene nanoribbons down to a 70 nm width. The electronic spectrum fragments into an unusual Landau levels pattern, characteristic of Dirac fermion confinement. The two-terminal magnetoresistance reveals the onset of magnetoelectronic subbands, edge currents and quantized Hall conductance. We bring evidence that the magnetic confinement at the edges unveils the valley degeneracy lifting originating from the electronic confinement. Quantum simulations suggest some disorder threshold at the origin of mixing between chiral magnetic edge states and disappearance of quantum Hall effect.

DOI: 10.1103/PhysRevLett.107.086601 PACS numbers: 72.80.Vp, 73.22.Pr, 75.47.−m

Introduction.—To benefit from the unusual transport properties of graphene [1,2] for future carbon-based nanoelectronics [3], the fabrication of clean materials has become a central issue. Of great concern is the design of graphene nanoribbons (GNRs), which allow some gap engineering [4]. The transverse confinement leads to 1D electronic subbands, whose details depend on the width and edge geometry of the ribbons [5].

In the presence of a strong perpendicular magnetic field, the anomalous quantum Hall Effect (QHE) develops in 2D graphene with unique properties widely discussed in the literature [6]. In nanoribbons, the electronic spectrum is predicted to evolve into magneto-electronic sub-bands resulting from a competition between magnetic and electronic confinement [2,5]. This is partly unveiled by anomalous Shubnikov–de Haas oscillations when the magnetic length becomes comparable to the ribbon width [7]. However, it is puzzling to note the lack of experimental evidence of Hall quantization in GNRs narrower than 200 nm [8–11]. Recent magnetotransport experiments in chemically derived [10] and lithographic [9,11] GNRs reported some signatures of chiral magnetic edge states revealed by a large positive magnetoconductance. However, in all these experiments, the conductance is far from being quantized and transport remains strongly diffusive, thus jeopardizing a convincing observation of the underlying Landau levels. Several sources of disorder are suspected to crosslink chiral edge currents, thus preventing QHE from developing [12]. Recent calculations also suggest a possible role of electron-electron interaction in the suppression of the conductance quantization [13]. A detailed characterization of Landau levels in GNRs thus remains to be accomplished.

In this Letter, we report two-terminal quantum Hall resistance measurements on GNR devices. We bring evidence of the Landau levels structure and of a singular electronic spectrum driven by the magnetic confinement and the edge symmetry at high fields. To rationalize these features, we simulate the spatial extension of the corresponding magnetic edge states and their distribution in presence of disorder.

Graphene devices are obtained by mechanical exfoliation of graphite onto $n^{++}\mathrm{Si}/\mathrm{SiO_2}$ (300 nm) substrates followed by *e*-beam lithography and thermal evaporation of the metallic electrodes. The graphene flakes are patterned into ribbons by oxygen plasma etching, using PMMA as an etching mask. A set of connected GNRs are prepared with width (W) ranging from 60 to 100 nm and length (L) from 350 to 800 nm. In what follows, we present extensive results for two devices (inset Fig. 1), sample A ($L = 350$ nm, $W = 100$ nm) and B

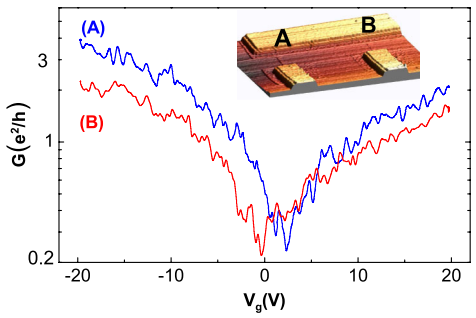

FIG. 1 (color online). Experimental $G(V_g)$ curves measured at 4.2 K on two GNR devices of width 100 and 70 nm (sample A and B). Inset: the AFM image of the devices.

($L = 750$ nm, $W = 70$ nm), having the hallmarks of the overall samples.

After thermal annealing in vacuum, the measured conductance $G(V_g)$ at 4.2 K (Fig. 1) exhibits a minimum in correspondence of the charge neutrality point (CNP) at relatively low back-gate potential $V_g = V_{\mathrm{CNP}} = 2.5$ V and -0.5 V for samples A and B, respectively, thus pinpointing a negligible residual doping. From a numerical calculation of the electrostatic coupling between the ribbons and the back-gate ([14]), the carrier density is estimated as $n(m^{-2}) \approx 1.5 \times 10^{15} \times (V_g(\mathrm{V}) - V_{\mathrm{CNP}})$ while the Fermi energy scales as $E_F(\mathrm{meV}) \approx 40 \times \sqrt{V_g(\mathrm{V}) - V_{\mathrm{CNP}}}$. From the $G(V_g)$ curves, and assuming a contact resistance in the range 1–4 kΩ [15], we infer an electronic mean free path $\ell_m \approx 50$–120 nm (80–120 nm) for sample $A(B)$ at $V_g = -20$ V. In both cases, $l_m \sim W$ and $L/l_m \approx 2$–7, which suggests a nearly quasiballistic transport regime. The good quality of the samples is also confirmed by the estimated large field effect mobility at 4.2 K $\mu_{A(B)} \approx 1200(3500)$ cm^2/(V s), and by the Fabry-Perot conductance modulations observed at 2 K.

Under a perpendicular magnetic field, the two-terminal resistance shows a nontrivial sample-shape dependent profile with fingerprints of both the quantized Hall resistance for filling factors $\nu(n_e h/eB) = 4(n + 1/2)$ and the longitudinal resistance for intermediate ν values [16]. Figure 2 shows the two-probe MR up to 55 T at various V_g for sample A. An oscillatory behavior of the resistance along with quantized minima ($h/6e^2$) and resistance plateaus ($h/2e^2$) are clearly visible. The MR plot as a function of the inverse magnetic field shows typical Shubnikov–de Haas oscillations [17]. However, a strong departure from the $1/B$ periodicity is observed for large numbers of occupied Landau levels N (inset, Fig. 2 circle marks). The linearity and its deviation above $N \approx 9$ are well reproduced by the calculation of $N(1/B)$ in the frame of semiclassical Bohr-Sommerfeld quantization rule with a hard-wall confinement (blue line). From the Eq. (1) in [17], we infer an effective width of 90 nm, close to the nominal one (100 nm), and a cyclotron radius ($l_c = k_F \hbar/eB$) of about 45 nm when entering the sublinear regime. This is a convincing signature that the electronic confinement starts to overcome the magnetic one when the cyclotron radius becomes larger than $W/2$.

Figure 3 shows the conductance profiles of the two GNRs as a function of the filling factor. The curves are deduced from the MR experiments, i.e., a constant charge density along with a pulse field sweep, meaning an increase of the Landau energy broadening versus ν. For sample A [Fig. 3(a)], a clear $2G_0$ Hall plateau (with $G_0 = 2e^2/h$) is observed at $\nu = 2$, thus providing direct evidence of a single layer graphene. For larger incompressible charge densities, at $\nu = 6, 10, \ldots$, only maxima of conductance develop instead of the expected $(6, 10, \ldots)G_0$ plateaus. This overall behavior is consistently described in the context of the conformal invariance of the conductance, where the distortion of the plateau is driven by the device aspect ratio $\xi = L/W$. Following the theory developed in [16], we reasonably well simulate our data for $\xi_{\mathrm{fit}} = 4.1$ (to be compared to $\xi_{\mathrm{exp}} = 3.5$) and a broadening $\Delta\nu \approx 0.84$ and 1.05 around $\nu = 2$ and 6, respectively, [Fig. 3(a), dashed line]. The larger broadening at higher filling factor is therefore responsible for the shrinkage of the $6G_0$ quantized state.

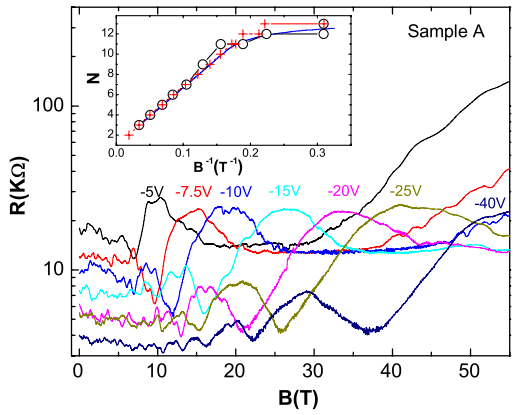

FIG. 2 (color online). Two-probe perpendicular MR measured at 4.2 K on sample A, for selected V_g. The inset shows anomalous $1/B$ Shubnikov-de Haas oscillations with circle marks indicating the number of occupied Landau levels N as a function of the $1/B$ locations deduced from the MR curve at -40 V. The red crosses are the $N(1/B)$ simulated data from the band structure [Fig. 5(a), inset]. The blue curve is the calculated $N(1/B)$ from [17].

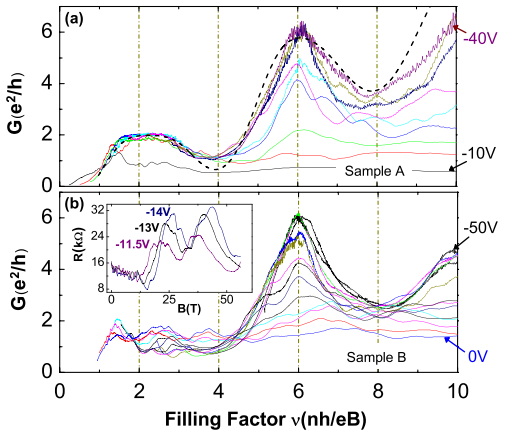

FIG. 3 (color online). (a) Experimental MC of sample A versus the filling factor deduced from the MR curves at selected V_g, from -40 V (top) to 0 V (bottom), by step of 5 V. The dashed line is the simulated $G(\nu)$. (b) The same for sample B at different V_g from -50 V (top) to 0 V (bottom), by step of 5 V. Inset: the singular MR curves at different V_g exhibiting a double resistance peak when E_F crosses the $n = 1$ Landau level.

Despite such an agreement, several intriguing experimental features demand further considerations. (i) The resistance peaks preceding the $h/2e^2$ plateau on sample A (i.e. corresponding to the crossing of the $n = 1$ Landau level) appear drastically enlarged for the MR curves at larger V_g (Fig. 2). (ii) Surprisingly, the Hall conductance of sample B, which is 30% narrower, does not present a well-defined $2G_0$ plateau even though the $6G_0$ quantization at $\nu = 6$ is preserved [Fig. 3(b)]. The suppression of the $2G_0$ conductance plateau goes along with a well-marked splitting and broadening of the resistance peak that develops before the expected plateau [Fig. 3(b) inset]. (iii) Both samples exhibit a gradual suppression of the $6G_0$ conductance at $\nu = 6$ as V_g decreases (Fig. 3).

For a deeper understanding of the MR curves and the related Landau levels pattern, we consider the magnetic field dependent band structure of two armchair ribbons (aGNRs) of width $W \approx 100$ and 70 nm. Because of the rather large W, the following discussion does not depend on the exact number of dimer lines that compose the ribbons. Figure 4 shows the band structures of the narrowest aGNR around the CNP at $B = 0$ and 50 T, obtained on the basis of our single-orbital per atom nearest-neighbor tight-binding description [5]. Note that the armchair boundary conditions entails the valley degeneracy lifting already at $B = 0$. As the magnetic field rises, magnetic and spatial confinement starts competing, with a progressive increase of the bottom of the bands and the flattening of their central region; see Fig. 4(b). This is an indication of the development of Landau levels. The magnetic confinement in the region of the bulk is so strong that these states do not feel the effect of the edges and they are valley-degenerate as in 2D graphene. However, when moving away from the bulk (i.e., at higher $|k|$ in the Brillouin zone) the effect of the edges becomes important again. The band energy rises (this corresponds to the formation of chiral edge channels) and the valley degeneracy is lost. In fact, when the plateau of a Landau level ends, one of the two bands rises while the other one first decreases and then rises again, see the blue circles in Fig. 4(b). The magnetic field dependence of the minimum energy of each subband is plotted in Fig. 5 (black solid and dashed lines). Above 10 T, they start to scale as $\sqrt{B}$, as for 2D graphene. However, the valley degeneracy breaking is enhanced since the propagating states become more confined along the armchair edges of the ribbon.

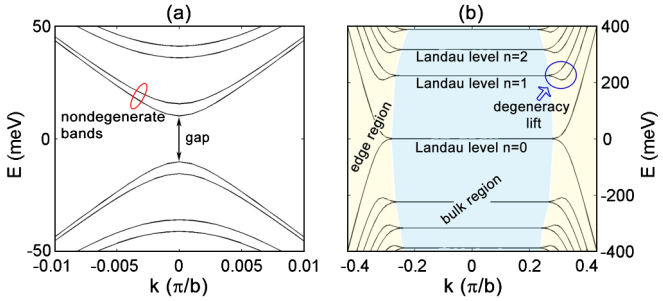

FIG. 4 (color online). Band structure of a 70 nm wide aGNR around the CNP at (a) $B = 0$ and (b) $B = 50$ T.

To relate the transport oscillations with the underlying band structure, we compare the intersection of the Fermi energy and the magneto-subbands spectrum with the locations of the maxima of the experimental resistance $R(B)$, in red curves. Figs. 5(a) and 5(b) depict the sample A at two different doping levels while Fig. 5(c) is for sample B (See [17] for additional data). Assuming a constant E_F (horizontal dashed lines), a good agreement between the locations of the resistance peaks and the subband depopulation for high quantum numbers is observed at low fields [inset of Fig. 5(a) and corresponding red crosses in the inset of Fig. 2]. However, a mismatch gradually develops below $n = 2$, when decreasing the electrical doping level. It eventually reaches several Tesla for $n = 1$, as marked by vertical dashed lines in Figs. 5(b) and 5(c).

To shed light on this issue, we observe that, as in conventional 2D gas, the Fermi energy is not constant but varies to accommodate the carriers into the available

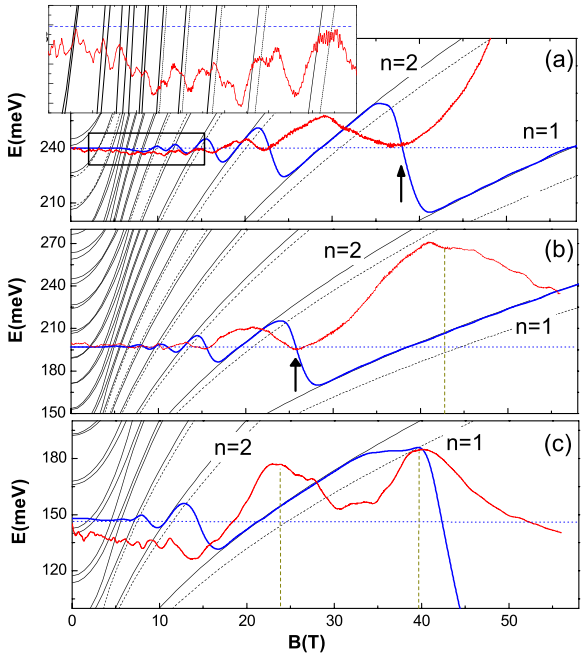

FIG. 5 (color online). (a) Simulated magnetoelectronic subbands versus B for the 100 nm wide aGNR compared to the experimental MR (red curve) at a selected E_F in blue. Black lines hold for the edge subbands at zero k. The dashed black lines correspond to the valley degeneracy lifting at nonzero k. The inset is a zoom at low field. (b) The same as in (a) for a lower doping level. Dark yellow vertical lines indicate the resistance peaks shifted to higher magnetic field due to the Fermi energy pinning at low n. (c) The same as in (a) for the 70 nm wide aGNR, exhibiting the valley degeneracy breaking.

subbands. This determines large oscillations of the Fermi energy at low n (see the blue lines in Fig. 5), with an evident pinning at the Landau levels at high magnetic fields. The Fermi energy oscillations provide a clear explanation of the shape of the MR curves in the high field regime. Indeed, the inflexion point of the $E_F(B)$ curves in between two successive Landau levels well matches with the minima of resistance; see the arrows in Figs. 5(a) and 5(b). Besides, the widening of the resistance peaks at larger V_g and their shift to high fields are a direct consequence of the stronger Fermi energy pinning onto the lowest index Landau levels. The absence of a sample B of a well-defined $2G_0$ plateau accompanying the splitting and the widening of the resistance peak also finds a natural explanation: The second maximum of resistance coincides with the changeover of E_F from the $n = 1$ Landau level (solid black line) to the second energy minimum at nonzero k (dashed black line). This is an unambiguous signature of the valley degeneracy lifting. It also suggests that the Landau pattern of sample B is potentially dominated by an armchair contribution at the edges, since the zigzag symmetry preserves the 2D graphene valley degeneracy. Note that such a valley degeneracy breaking induced by an hard-wall confinement of armchair type is already expected at 0 T. However, the rather low energy splitting and the presence of disorder make it unobservable in our zero field transport measurements. Interestingly, our interpretation suggests that the armchair contribution at edges is revealed through magnetic confinement, when the propagating states are strongly pushed to the ribbon edges. The key conditions for observation of the high field magneto fingerprints are a large enough energy splitting between the two sublevels and the pinning of the Fermi energy on the two states. Such conditions are borne out on sample B, which has a higher mobility and allows for a sharper valley degeneracy lifting with a higher density of states at the subband edges.

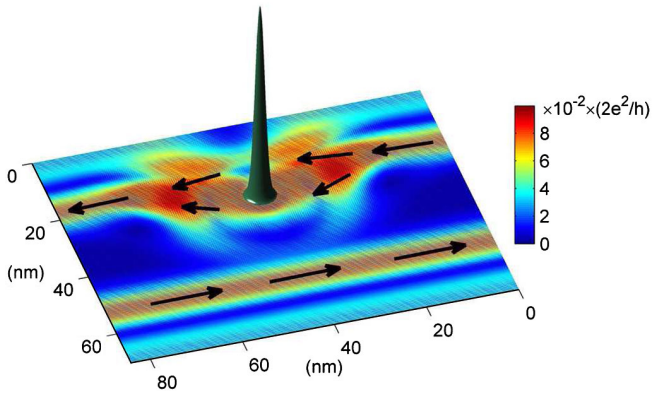

FIG. 6 (color online). Spatial distribution of the background spectral currents through a 70 nm wide aGNR at $\nu = 6$ ($E_F = 119$ meV and $B = 12$ T), in presence of a Gaussian potential with maximum strength $V = 1$ eV, mimicking a single charged impurity.

We finally comment on the gradual suppression of the $6G_0$ conductance at $\nu = 6$ when decreasing the back-gate voltage (Fig. 3). From a simulation of the spatial profile of the edge channels at $\nu = 6$ as a function of the magnetic field [17], we infer that the widening of the chiral currents when decreasing V_g cannot account for the suppression of the $6G_0$ conductance in case of defect-free ribbons. In fact they are still well separated by few tens of nanometers when the conductance starts to decrease. However, the introduction of disorder along the ribbon makes the chiral currents come significantly closer, thus facilitating backscattering. As a matter of illustration, Fig. 6 shows the leakage of edge currents (at $\nu = 6$) entailed by a single charged impurity for a 70 nm wide graphene ribbon.

Conclusion.—Our results unveil an unusual magnetic structure of graphene nanoribbons providing unambiguous fingerprints of Dirac fermion magnetic confinement, reinforcing the key role of edge symmetry. To support the proposed interpretation, it would be highly desirable to complement our data with structural information on the edges, for example, by Raman spectroscopy techniques [18]. Our quantum simulations also illustrate disorder-induced mixing of edge currents, at the origin of the observed degradation of the conductance quantization.

Sample preparations were achieved at LAAS. Part of this work is supported by EuroMagNET, contract No. 228043, the NANOSIM-GRAPHENE Project No. ANR-09-NANO-016-01 and the MAGBiSy Project No. ANR-08-JCJC-0034-01. A. C. acknowledges the support of Fondation Nanosciences via the RTRA Dispograph project.

[1] A. K. Geim and K. S. Novoselov, Nature Mater. **6**, 183 (2007).
[2] A. H. Castro Neto *et al.*, Rev. Mod. Phys. **81**, 109 (2009).
[3] F. Schwierz, Nature Nanotech. **5**, 487 (2010).
[4] M. Y. Han *et al.*, Phys. Rev. Lett. **98**, 206805 (2007).
[5] K. Wakabayashi *et al.*, Phys. Rev. B **59**, 8271 (1999); K. Wakabayashi, Phys. Rev. B **64**, 125428 (2001); A. Cresti *et al.*, Nano Res. **1**, 361 (2008).
[6] K. S. Novoselov *et al.*, Nature (London) **438**, 197 (2005); Y. B. Zhang *et al.*, Nature (London) **438**, 201 (2005); K. S. Novoselov *et al.*, Science **315**, 1379 (2007).
[7] N. M. R. Peres, A. H. Castro Neto, and F. Guinea, Phys. Rev. B **73**, 241403(R) (2006); C. Berger *et al.*, Science **312**, 1191 (2006).
[8] F. Molitor *et al.*, Phys. Rev. B **79**, 075426 (2009).
[9] J. B. Oostinga *et al.*, Phys. Rev. B **81**, 193408 (2010).
[10] J. Poumirol *et al.*, Phys. Rev. B **82**, 041413(R) (2010).
[11] J. Bai *et al.*, Nature Nanotech. **5**, 655 (2010).
[12] I. Romanovsky, C. Yannouleas, and U. Landman, Phys. Rev. B **83**, 045421 (2011); E. Prada, P. San-Jose, and L. Brey, Phys. Rev. Lett. **105**, 106802 (2010); C. Ritter, S. S. Makler and A. Latgé, Phys. Rev. B **77**, 195443 (2008).

[13] A. A. Shylau *et al.*, Phys. Rev. B **82**, 121410(R) (2010).
[14] Available at http://www.fastfieldsolvers.com
[15] X. Wang *et al.*, Phys. Rev. Lett. **100**, 206803 (2008).
[16] J. R. Williams *et al.*, Phys. Rev. B **80**, 045408 (2009); D. A. Abanin and L. S. Levitov, Phys. Rev. B **78**, 035416 (2008).
[17] See Supplemental Material at http://link.aps.org/supplemental/10.1103/PhysRevLett.107.086601 for technical details and additional experimental results.
[18] C. Casiraghi *et al.*, Nano Lett. **9**, 1433 (2009).